Journal of Power Sources 666 (2026) 239162

Contents lists available at ScienceDirect

Journal of Power Sources

journal homepage: www.elsevier.com/locate/jpowsour

Planar flexible micro-supercapacitors with high electrochemical performance over a wide temperature range

Na Chen [a], Guo-Tao Xiang [a], Rui-Dong Shi [a], Jia-Lei Xu [a], Aura Garcia [b], Raul D. Rodriguez [b], Jin-Ju Chen [a,*]

[a] School of Materials and Energy, University of Electronic Science and Technology of China, Chengdu, 610054, PR China
[b] Tomsk Polytechnic University, Lenina Ave. 30, Tomsk, 634034, Russia

HIGHLIGHTS

- Flower-like 1T-MoS_2 anchored on rGO was used to develop MSCs.
- A polyacrylamide/trehalose/LiCl hydrogel was developed as the MSCs' electrolyte.
- The MSCs achieved a high energy density and excellent cycling stability.
- The MSCs had exceptional flexibility and a wide temperature range adaptability.
- Inkjet-printed MSCs can be easily interconnected in series or parallel.

GRAPHICAL ABSTRACT

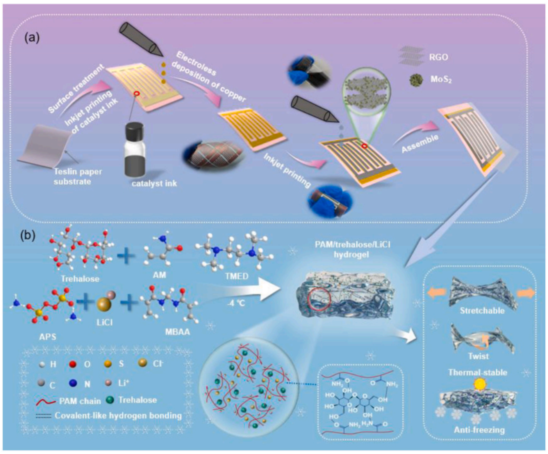

ARTICLE INFO

Keywords:
Inkjet printing
Planar micro-supercapacitor
Hydrogel electrolyte
Flexibility
Electrochemical performance

ABSTRACT

The pursuit of high energy density and exceptional reliability is critical for the advancement of micro-supercapacitors (MSCs). To enhance their electrochemical performance across a broad temperature range, innovative planar MSCs have been developed with flower-like 1T-phase MoS_2 anchored on reduced graphene oxide (RGO) as the electrode material. These MSCs are combined with a flexible polyacrylamide (PAM)/trehalose/LiCl hydrogel electrolyte. The self-assembled 1T-MoS_2/RGO hybrid structure endows the MSCs with a high energy density of 15.0 $mWh\cdot cm^{-3}$ and an impressive capacitance retention rate of 88.21 % after 8000 cycles at 20 °C. The non-covalent interactions between trehalose and PAM contribute to the MSCs' exceptional flexibility and wide temperature range adaptability, enabling operation from −30 °C to 80 °C. Moreover, taking advantage of the simplicity of inkjet printing, MSC devices can be easily interconnected in series or parallel to increase power output. These MSCs, with their enhanced temperature resilience, offer a promising strategy for broadening the application of flexible energy storage technologies.

---

* Corresponding author.
E-mail address: jinjuchen@uestc.edu.cn (J.-J. Chen).

https://doi.org/10.1016/j.jpowsour.2025.239162
Received 22 April 2025; Received in revised form 1 December 2025; Accepted 18 December 2025

1. Introduction

The exponential growth of wearable electronics has spurred the advancement of micro-energy storage devices capable of operating under harsh conditions [1–3]. Among various types of miniature energy storage devices, micro-supercapacitors (MSCs) have garnered significant interest due to their superior power density, rapid charging and discharging capabilities, and excellent cycle stability [4]. Traditional MSCs with a sandwich structure exhibit limited flexibility because of their thickness, whereas fiber-shaped MSCs are intricate to fabricate and challenging to scale up in production [5]. In contrast, planar MSCs equipped with interdigitated electrodes are thin and flexible, making them highly suitable for integration into wearable electronic systems [6].

Manufacturing techniques for planar MSCs, including screen printing [7,8], vacuum extraction [9,10], photolithography [11], and laser processing [12], often involve complex procedures or necessitate costly equipment [13]. However, inkjet printing stands out as a cost-effective and eco-friendly alternative. This digital printing method eliminates the need for molds, facilitates scalability, and enables the precise fabrication of diverse patterns [14,15]. Integrating nanomaterials with outstanding charge storage capabilities into low-cost manufacturing processes is crucial for achieving high energy density in MCSs. MoS_2 has a layered structure composed of S-Mo-S atomic sheets bonded by weak van der Waals interactions, conferring a distinctive two-dimensional character. This structure furnishes a substantial theoretical surface area conducive to charge storage and facilitates the generation of few-layered materials amenable to inkjet printing via ultrasonic exfoliation [16,17]. Moreover, while the 2H phase of MoS_2 exhibits semiconducting properties, the metallic 1T phase boasts high conductivity, making it an optimal choice for energy storage in batteries and supercapacitors [18,19]. Strategies such as morphology control, phase engineering, and the creation of composite materials with enhanced conductivity have been employed to advance the use of MoS_2 in supercapacitors [20]. While pure graphene offers excellent intrinsic conductivity, RGO possesses a rich surface chemistry (with functional groups such as hydroxyl, epoxy, carbonyl, and carboxyl groups) that confers two key advantages: (1) excellent hydrophilicity, which facilitates the uniform formation of composites with metal sulfides [R1, R2], and (2) these functional groups serve as anchoring sites, enabling intimate contact and strong interfacial bonding between the RGO nanosheets and the flower-like 1T-MoS_2 nanostructures [21]. Therefore, the synergistic combination of RGO and 1T-MoS_2 is anticipated to significantly enhance the electrochemical performance of MSCs, primarily by leveraging the synergistic effects between these materials to optimize charge storage and capacitive behavior.

Developing an electrolyte that enables stable operation of the device across an ultra-wide temperature range is crucial, and it should exhibit excellent compatibility with the electrode material [22]. In recent years, hydroxyl-rich hydrogel electrolytes have demonstrated significant application potential in flexible energy storage systems due to their outstanding flexibility, high safety, and excellent water retention capabilities. Their stable porous architecture facilitates efficient ion transport, enhancing the electrochemical performance of these devices. However, the substantial water content in electrolytes can lead to freezing at low temperatures or evaporation at low/high temperatures, degrading electronic conductivity and mechanical integrity and impacting device performance. This severely limits device reliability in real-world environments [23–25]. To address this challenge, research has explored incorporating freeze-resistant components such as ethylene glycol, dimethyl sulfoxide, or zwitterionic ions. Alternatively, introducing polymer networks capable of forming non-covalent interactions with hydrogel polymers aims to enhance mechanical properties and thermal stability [26]. However, many organic additives pose toxicity concerns and may inhibit ion transport at low temperatures due to increased system viscosity. Although ionic liquids offer high ionic conductivity, their high costs can limit their broader adoption [27]. Consequently, developing novel hydrogel electrolyte systems that are environmentally friendly, cost-effective, and adaptable across wide temperature ranges remains a critical research direction in this field. Incorporating trehalose, renowned for its biocompatibility and the presence of numerous active groups, along with high concentrations of inorganic salts, into hydrogel formulations is identified as a promising strategy to enhance their mechanical robustness, temperature tolerance, and ionic conductivity, which are pivotal for the advancement of energy applications.

In this study, we fabricated a composite material featuring flower-like 1T-MoS_2 attached to RGO, and combined with the inkjet printing to prepare the interdigital electrode. Following this, we assembled planar MSCs with a PAM/trehalose/LiCl hydrogel electrolyte that operates across an extensive temperature range from $-30\ ^\circ C$ to $80\ ^\circ C$. The 1T-MoS_2/RGO composite leverages the large specific surface area of 1T-MoS_2 and the high electrical conductivity of RGO, resulting in MSCs with outstanding electrochemical performance. The non-covalent interactions and solvation within the PAM/trehalose/LiCl hydrogel electrolyte confer the assembled MSCs with adequate flexibility and temperature resilience. The MSCs exhibit an exceptional energy density across a broad temperature range, and the maximum specific capacitances at $20\ ^\circ C$, $80\ ^\circ C$ and $-30\ ^\circ C$ at a scanning rate of $5\ mV\ s^{-1}$ are 47.4, 60 and 10.1 mF cm^{-2}, respectively. Moreover, the capacity retention within this temperature range exceeded 75.5 %, indicating desirable cycling stability.

2. Results and discussion

2.1. Characterizations of electrode materials

We fabricated Cu interdigital electrodes (comparable to noble metals, ensuring low-cost and scalable fabrication compatible with flexible substrates) on Teslin paper, serving as current collectors with an electrical conductivity of approximately $4 \times 10^7\ S\ m^{-1}$, using a combination of inkjet printing and electroless plating, as previously described [28]. MoS_2/RGO ink was loaded into the cartridge of an Epson L130 desktop printer. The ink was then printed onto the Cu current collectors according to the pattern depicted in Fig. 1a. Subsequently, PAM/trehalose/LiCl hydrogels (Fig. 1b) synthesized by free radical polymerization were used to assemble MSCs as electrolytes.

SEM and TEM were employed to investigate the morphology of the fabricated samples. Fig. 2a and b illustrate that the synthesized MoS_2 exhibits nanoflower structures and is subsequently embedded in nanosheets within RGO layers. The nanoflower morphology of MoS_2 significantly increases the specific surface area, offering abundant active sites for charge storage. The MoS_2 nanoflowers are interconnected through the RGO matrix, establishing an efficient electron transport network. EDS elemental mapping delineates the distribution of Mo, S, and C within the MoS_2/RGO samples, with each element precisely localized to its respective areas, shown in Fig. 2c. TEM images in Fig. 2d and e further confirm the flower-like morphology of MoS_2 integrated within the lamellar RGO structure, in agreement with the SEM observations, verifying the successful formation of the MoS_2/RGO composite. Fig. 2f presents a high-resolution TEM image of the MoS_2/RGO composite, which displays lattice fringes with a spacing of 0.96 nm corresponding to the (002) crystal plane of MoS_2. Furthermore, the selected area electron diffraction (SAED) pattern in Fig. 2g exhibits distinct diffraction rings, which are attributed to the MoS_2 (002), (101), and (106) crystal planes, confirming the successful synthesis of the MoS_2 material.

Raman spectra was utilized to investigate the phase composition of the MoS_2/RGO composite, as depicted in Fig. 3a. The Raman spectra exhibits distinct peaks at 141 cm^{-1} (J_1), 234 cm^{-1} (J_2), and 335 cm^{-1} (J_3), which are characteristic of the 1T phase in MoS_2. Additionally, the E_{1g} peak at 280 cm^{-1} confirms the octahedral coordination of molybdenum in 1T-MoS_2 [29]. The weak E^1_{2g} peak observed at 378 cm^{-1} suggests the presence of a minor amount of the 2H phase within the sample [30]. The composites also display the characteristic D and G Raman peaks associated with graphene, indicating a homogeneous mixture.

The phase composition of the synthesized MoS_2 samples was characterized by XRD, as shown in Fig. 3b. The observed diffraction peaks match the (100), (102), (006), and (110) crystal planes of MoS_2, which are indexed against the standard card (JCPDS No. 37–1492) [31]. In the low-angle region, the peak at 9.3° is assigned to the (002) plane of the 1T phase, while the peak at 14.1° corresponds to the (002) plane of the 2H phase. According to Bragg's law, a larger diffraction angle indicates a smaller lattice constant for a constant X-ray wavelength. Consequently, the increased interlayer spacing in the MoS_2 sample, as evidenced by the diffraction data and consistent with the TEM finding, promotes the rapid diffusion of ions.

XPS analysis was conducted to determine the valence states and elemental composition of the MoS_2/RGO composite, as depicted in Fig. 3c. This analysis confirmed the presence of Mo, S, and C elements. The high-resolution Mo 3d XPS spectrum displays five distinct peaks at 231.8, 228.6, 232.7, 229.5, and 226.3 eV (Fig. 3d). These peaks can be attributed as follows: Mo^{4+} $3d_{3/2}$ and $3d_{5/2}$ orbitals of the 1T phase are observed at 231.8 and 228.6 eV, respectively, while the corresponding orbitals of the 2H phase are found at 232.7 and 229.5 eV, and the peak at 226.3 eV corresponds to the S 2s orbital [32]. Notably, the binding energy of the peaks associated with the 1T phase is 0.9 eV lower than those of the 2H phase, indicative of Fermi level shifts due to the occupation of additional electrons in the d orbitals during the phase transition [33]. The S 2p spectrum in Fig. 3e is deconvoluted into four peaks, which correspond to the S 2p3/2 and S 2p1/2 orbitals for both the 1T and 2H phases, with binding energies at 161.4, 162.6, 162.1, and 163.8 eV, respectively [19,34].

The MoS_2/RGO composite was formulated into an ink, and its hydrophilicity was evaluated using contact angle measurements on Teslin paper, as shown in Fig. 3f. The ink exhibits contact angles of 60.89°, 60.67°, and 59.90° over three trials, indicating its favorable hydrophilic nature and being conducive to the uniform distribution of the ink. Zeta potential measurements were performed twice, resulting in values of −46.9 mV and −48.7 mV, which confirm the ink's stability. Additionally, the Tyndall effect is observed in the MoS_2/RGO ink. Even after three months (refer to Fig. S1), this effect is still significant, suggesting a consistent and stable dispersion of the MoS_2/RGO composites within the ink medium.

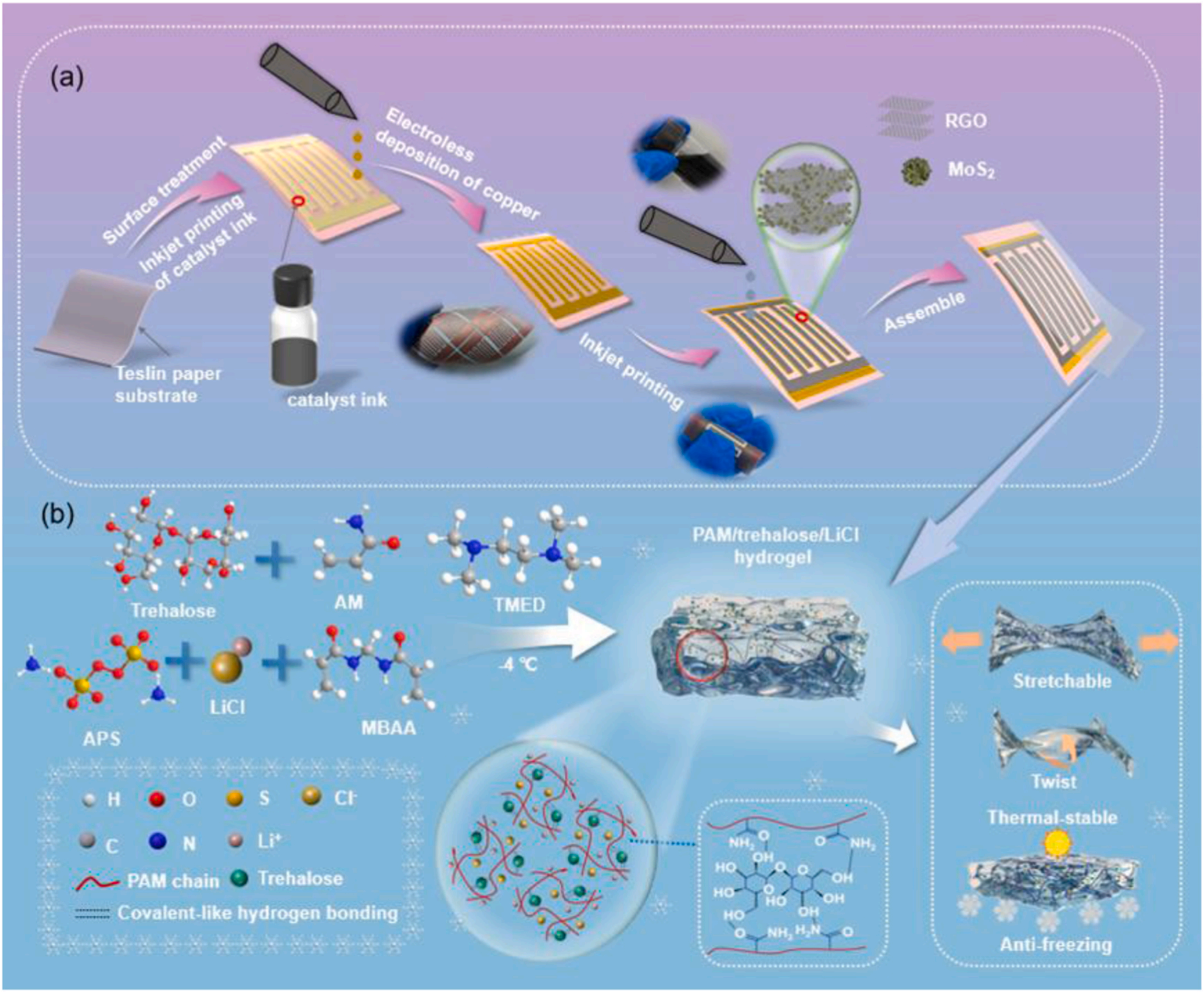

Fig. 1. Schematic diagram of MSCs manufacturing process (a) and PAM/trehalose/LiCl hydrogels (b).

2.2. Properties of hydrogels

Fig. 1b depicts the synthetic mechanism of the PAM/trehalose/LiCl hydrogel. Initially, a trehalose solution was mixed with LiCl electrolyte and AM monomer. Subsequently, APS was added as the initiator, and MBAA was introduced as the cross-linker. TMED was introduced as a catalyst into the mixture while stirring at −4 °C. TMED facilitates the formation of free radicals from ammonium persulfate, thereby accelerating the polymerization of the polyacrylamide gel. The freeze-dried hydrogels were characterized using SEM, as shown in Fig. S2a. The SEM image reveals a three-dimensional porous structure, resulting from the salting-out effect caused by LiCl [35]. This structure facilitates rapid transport of ions (Cl^-, Li^+) and imparts significant flexibility to the hydrogel electrolyte. Fig. S2b displays the FTIR spectra of PAM and PAM/trehalose hydrogels. The characteristic peaks of PAM hydrogel at 3342 cm^{-1} and 1654 cm^{-1} correspond to the N-H stretching and C=O stretching vibrations, respectively. In the PAM/trehalose hydrogel, these peaks are red-shifted to 3332 cm^{-1} and 1649 cm^{-1} for the N-H and C=O vibrations, respectively, indicating the presence of hydrogen bonding between trehalose and PAM molecular chains.

The mechanical robustness of hydrogel electrolytes is vital for their application in wearable energy storage devices. To assess this, we

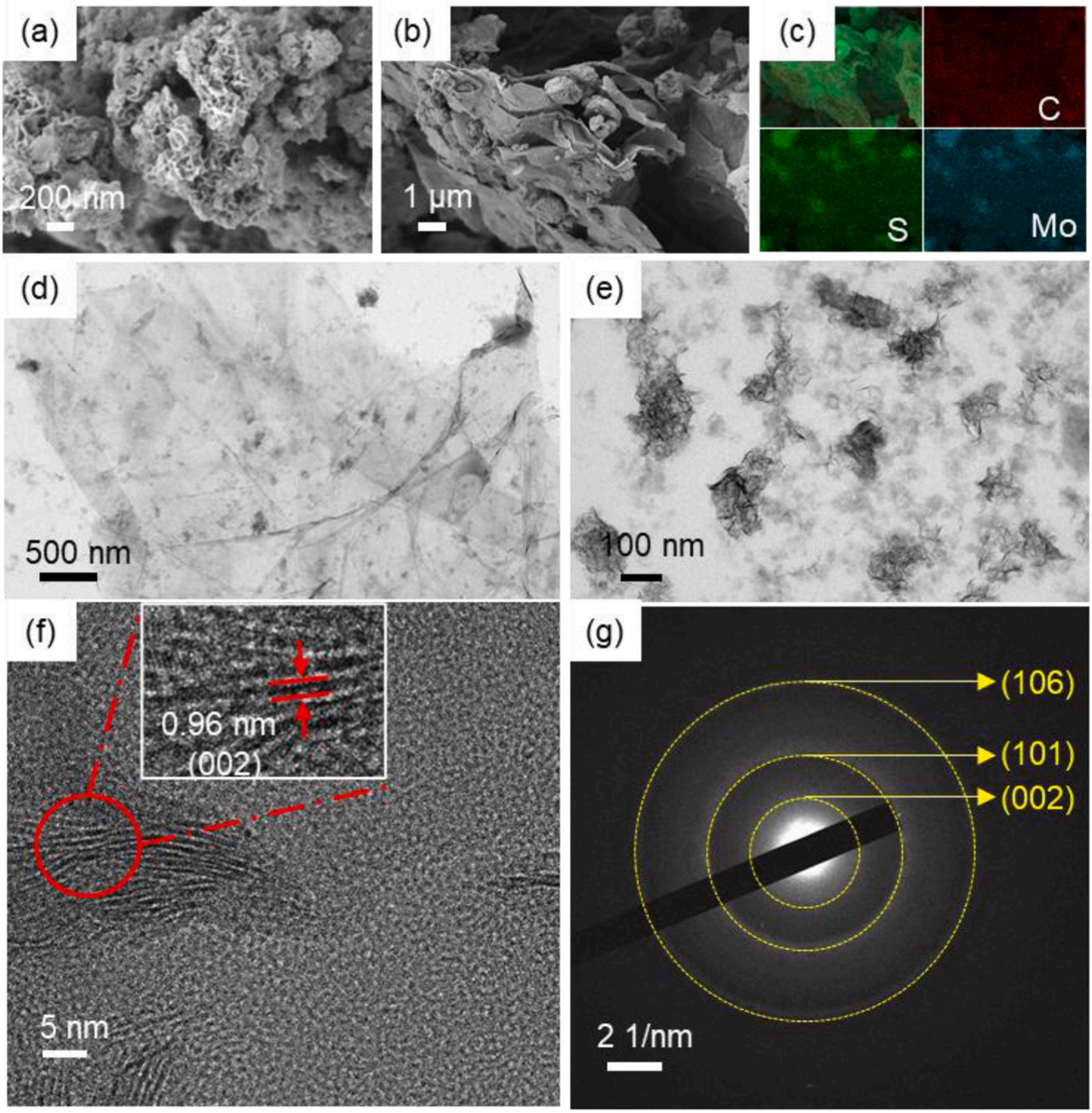

Fig. 2. SEM images of (a) MoS_2 and (b) MoS_2/RGO. (c) Elemental mapping images, (d, e) TEM images, (f) high-resolution TEM image, and (g) SAED pattern of the MoS_2/RGO sample.

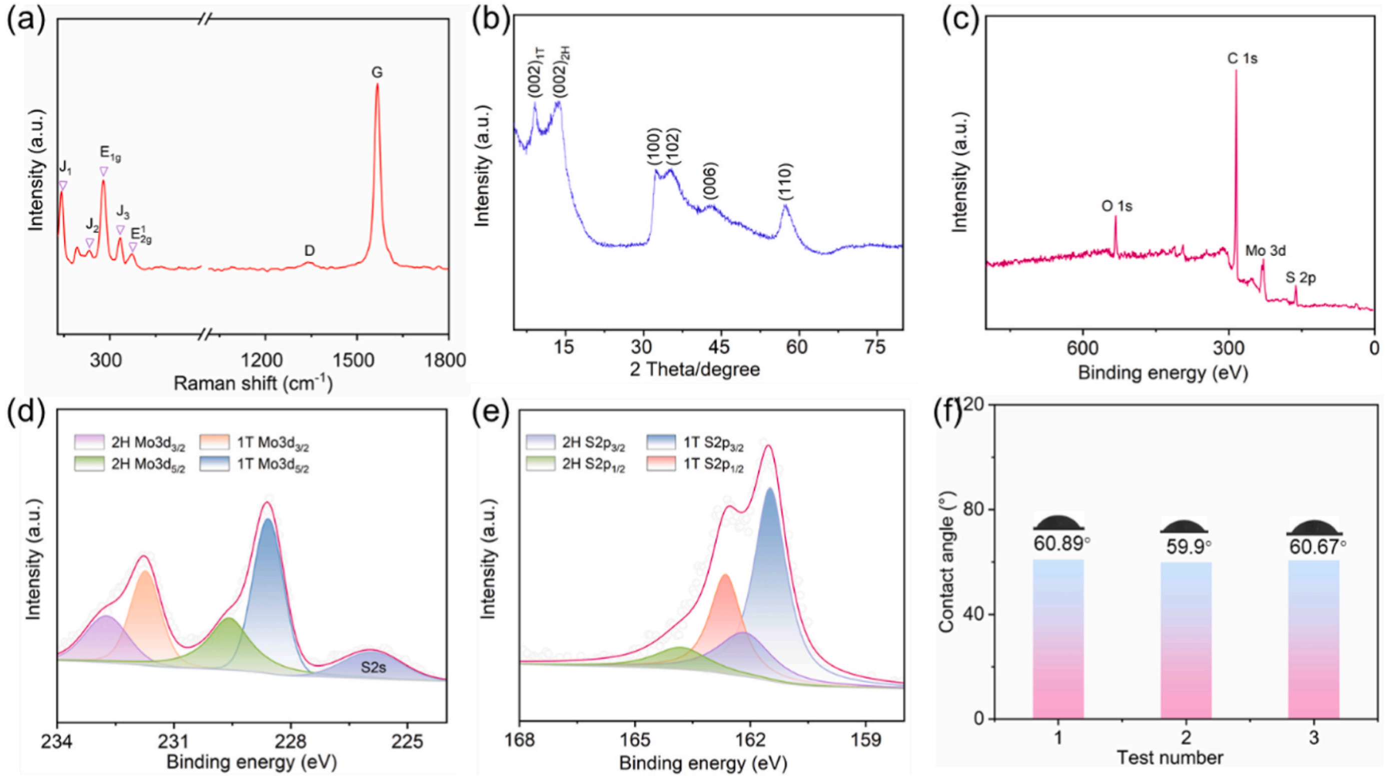

Fig. 3. (a) Raman spectra of the MoS_2/RGO composite. (b) XRD pattern for MoS_2. XPS spectra for the MoS_2/RGO composite, including (c) the survey spectrum and high-resolution XPS spectra of (d) Mo 3d and (e) S 2p. (f) The contact angle for the MoS_2/RGO ink.

conducted tensile testing on our hydrogel. Fig. 4a illustrates the stress-strain curve of the PAM/trehalose/LiCl hydrogel, showcasing its exceptional elongation at break (522.6 %) and tensile strength (191.86 kPa), significantly surpassing the PAM/trehalose (460 %, 170 kPa) and PAM/LiCl (314.6 %, 130 kPa) hydrogels. The comparison of Young's modulus and toughness of the three hydrogels is shown in Fig. 4b. The PAM/trehalose/LiCl hydrogel demonstrates Young's modulus of 156 kPa and toughness of 748 kJ m^{-3}, outperforming the PAM/trehalose (136 kPa, 553 kJ m^{-3}) and PAM/LiCl (105 kPa, 269 kJ m^{-3}) hydrogels. The enhanced mechanical properties of the PAM/trehalose/LiCl hydrogel can be attributed to the incorporation of trehalose, whose abundant hydroxyl groups form hydrogen bonds with the PAM polymer chains. This interaction increases the interconnectivity between PAM chains and trehalose molecules, reinforcing the network structure of the hydrogel. Additionally, the presence of LiCl significantly improves the elongation at break, tensile strength, Young's modulus, and toughness of the hydrogel. These superior mechanical attributes of the hydrogel are due to the three-dimensional porous structure, which provides flexibility, and the strong hydration of Li^+ ions that promote non-covalent interactions [36]. In addition, Li^+ and Cl^- ions disrupts intermolecular interactions between water molecules, reducing free water content within the hydrogel while increasing bound water content. This ensures the hydrogel electrolyte maintains adequate water content, resulting in excellent flexibility.

To evaluate the mechanical properties of the PAM/trehalose/LiCl hydrogels, tensile tests were performed at various strains (50 %, 100 %, 200 %, 300 %, and 400 %) and under cyclic loading-unloading at 100 % strain, as depicted in Fig. 4c and d. The hydrogels show exceptional resilience across the range of tensile tests in Fig. 4c. The loading and unloading curves in Fig. 4d almost coincide completely, with a minimal hysteresis area, signifying the hydrogels' remarkable self-recovery and elasticity. This superior mechanical performance can be credited to the dynamic breaking and reformation of reversible intermolecular bonds. The PAM/trehalose/LiCl hydrogel displays remarkable tolerance to deformations such as knotting, twisting, and stretching, as illustrated in Fig. 4e, and remains intact when supporting a 1 kg load, as shown in Fig. S3. Additionally, the versatility of the hydrogel is demonstrated by its capability to firmly adhere to various substrates, including glass, steel, and ceramics, as seen in Fig. 4f.

The ionic conductivity of hydrogel electrolytes is crucial for the electrochemical performance of supercapacitors (MSCs) made using these electrolytes. To assess this, EIS measurements were performed on PAM/trehalose/LiCl hydrogels with different LiCl concentrations (3 M, 6 M, 9 M, and 12 M), as shown in Fig. 4g. The corresponding ionic conductivities are presented in Fig. S4 and Table S1. The bulk impedance of the hydrogels decreases with higher LiCl content, reaching its lowest point at 6 M, where the ionic conductivity peaks at 23.6 mS cm^{-1} (calculated from equation 2). At concentrations beyond 6 M, the formation of ionic clusters hinders ion mobility, causing a decrease in the conductivity of the hydrogel electrolytes. Therefore, in the subsequent electrochemical testing, the LiCl concentration in the PAM/trehalose/LiCl hydrogels is set at 6 M.

The moisture retention capability of hydrogel electrolytes is essential for the operation of MSCs under extreme conditions. To quantify this retention, hydrogels with varying LiCl concentrations were exposed to an oven at 80 °C, and their weight was monitored hourly. The moisture retention rate was calculated using Equation 1. Fig. 4h illustrates that the mass retention of the hydrogels after 10 h is directly proportional to the LiCl concentration. However, the retention rate declines when the LiCl concentration exceeds 6 M. The hydrogel with 6 M LiCl achieves a retention rate of 87.9 %, significantly outperforming the other electrolytes. The LiCl hydration enhances the interaction between the hydrogel and water molecules, reducing the amount of free water and increasing bound water, thus improving retention. Nevertheless, ionic clustering reduces the interaction at higher LiCl concentrations, increasing the free water. Additionally, incorporating trehalose into the 6 M LiCl hydrogels significantly enhances their retention, likely due to the hydrogen bonding between the trehalose and polymer chains slowing water loss.

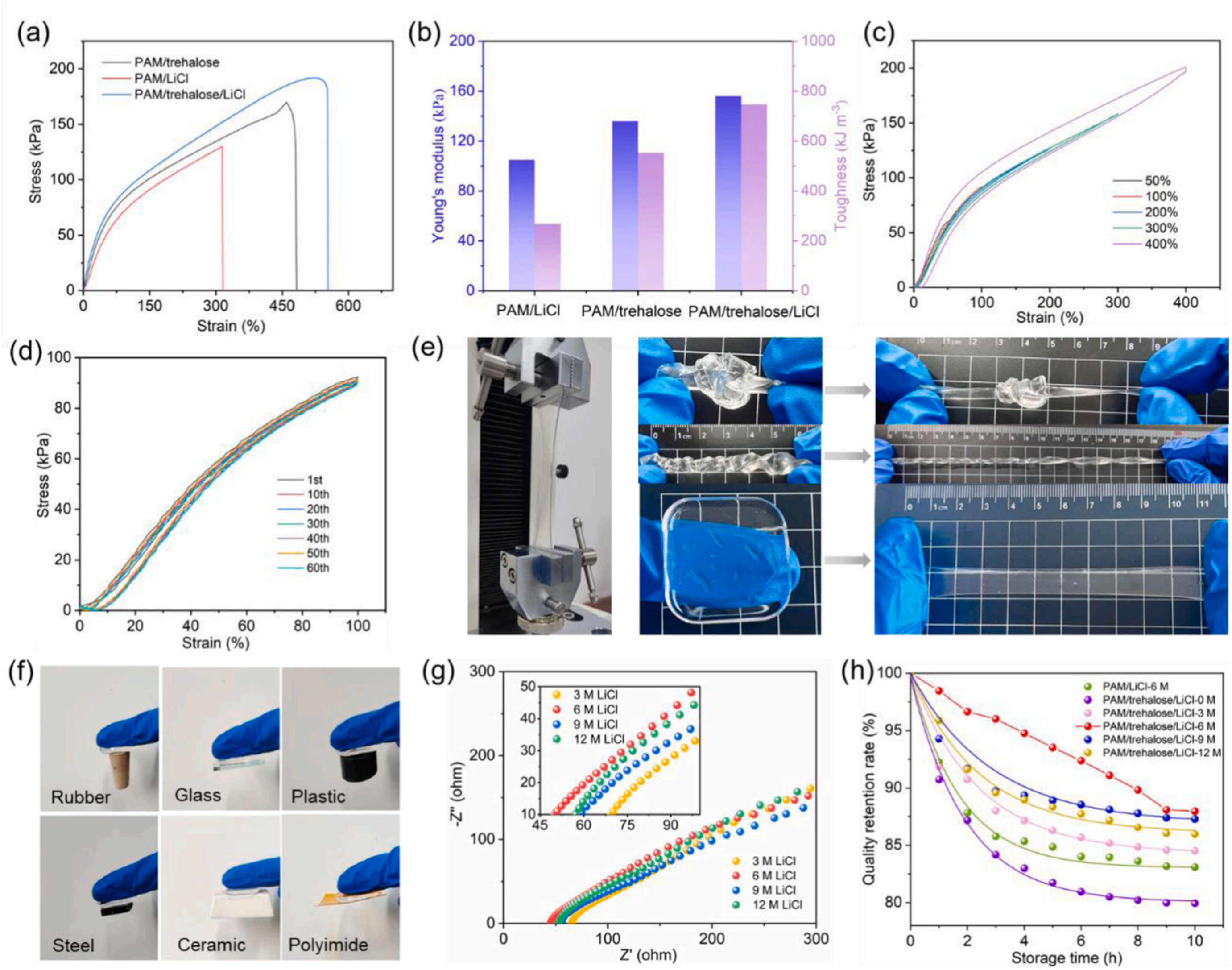

Fig. 4. Characteristics of PAM/trehalose/LiCl hydrogels: (a) Stress-strain curves, (b) Young's modulus and toughness values, (c) continuous cyclic tensile testing (50–400 %), and (d) continuous cyclic loading-unloading curves at 100 % strain for 60 cycles. (e) Optical photographs of PAM/trehalose/LiCl hydrogels undergoing stretching and twisting. (f) Photographs of PAM/trehalose/LiCl hydrogels adhered to various substrates. (g) EIS spectra for hydrogels with different LiCl concentrations. (h) Quality retention rate plots for hydrogels with different LiCl concentrations after exposure to an oven at 80 °C.

As shown in Fig. S5, the hydrogels also retain flexibility after 10 h at 80 °C. This robust moisture retention expands the potential applications of these hydrogels.

2.3. *Electrochemical properties of MSCs*

The MoS_2/RGO ink was deposited on Teslin paper using inkjet printing, with 30 printing passes to create interdigital electrodes, as shown in Fig. 5a and S6. The GCD curves of MoS_2/RGO electrode is shown in Fig. S7, demonstrating an excellent specific capacitance of 408.8 F g^{-1} at a current density of 1 A g^{-1}. MSCs were then constructed using the PAM/trehalose/LiCl hydrogel with 6 M LiCl as the electrolyte. The electrochemical performance of the MSCs was assessed using an electrochemical workstation. The MSCs were operated within a voltage window of 0–0.6 V. Fig. S8 and 5b present the CV curves for MSCs without and with a copper collector, respectively. MSCs equipped with copper collectors exhibit lower internal resistance, which enhances the carrier's mobility. To quantify the contribution of the copper collector to the capacity of MSCs, CV curves were compared for MSCs based on copper interdigital electrodes and for those based on MoS_2/RGO interdigital electrodes with and without copper collectors, at a scan rate of 100 mV s^{-1}, as shown in Fig. 5c. This comparison reveals that the CV loop area for the pure copper MSCs is small, indicating a negligible capacity contribution. Conversely, the copper collector presence significantly boosts the areal capacity of the MSCs, as demonstrated in Fig. 5d, reaching an area capacitance of 47.4 mF cm^{-2} (calculated according to equation 3) at 5 mV s^{-1}. The GCD curves at different current densities (Fig. 5e) exhibit symmetric and triangular profiles, indicating high Coulombic efficiency of MSCs based on MoS_2/RGO with copper collector.

Cycling stability is a critical criterion for the practical application of MSCs. The optimal MSCs demonstrate an impressive capacity retention of 88.21 % and a high Coulombic efficiency of 96.19 % after undergoing 8000 cycles at 0.3 mA cm $^{-2}$, as depicted in Fig. 5f, underscoring their exceptional cycling stability. Using Equation 4, the MSCs exhibit an areal energy density of 2.4 μWh cm^{-2}. Furthermore, the MSCs exhibit a volume energy density of 15.0 mWh cm^{-3}, taking into account the printed MoS_2/RGO layer thickness (1.58 μm), as described in Fig. S9, which is notably superior to the energy densities reported for most of MSCs in the literature, owing to the high ionic conductivity provided by LiCl and the excellent interfacial contact between the hydrogel and the electrode. Notably, these studies employed identical or similar electrode

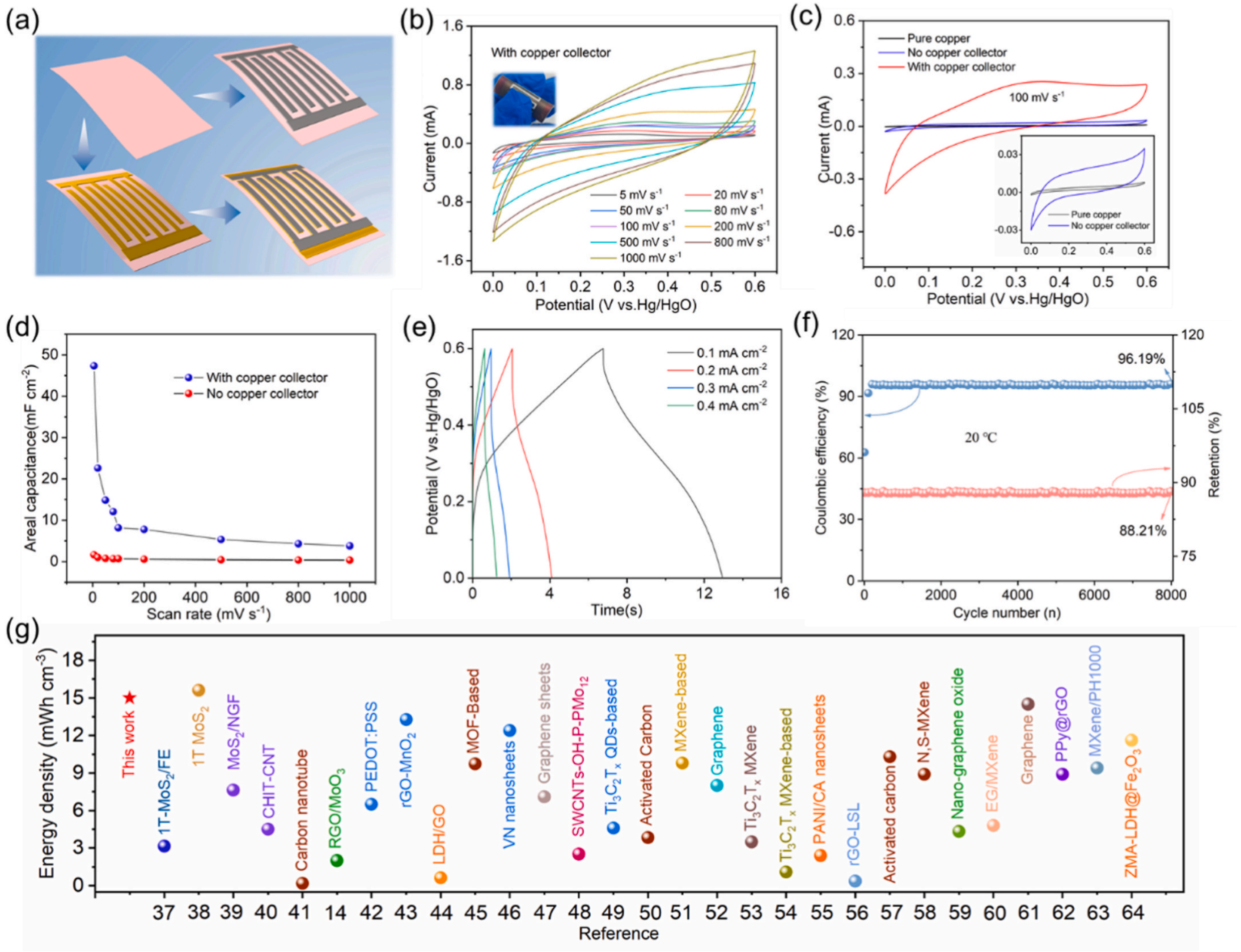

Fig. 5. (a) The schematic diagram for preparing MSCs. CV curves of MSCs (b) with copper collector at various scan rates. (c) CV curves of MSCs assembled from pure copper interdigital electrodes, MoS_2/RGO interdigital electrodes without copper collector, and MoS_2/RGO interdigital electrodes with copper collector electrodes at a scan rate of 100 mV s^{-1}. (d) The areal capacitance of MSCs with and without copper collector. (e) GCD curves of MSCs with the copper collector. (f) Cycling performance of the MSC at 0.3 mA cm^{-2}. (g) Comparison of volume energy density between our MSC and other literature reports.

materials as active components but utilized different electrolyte systems (including other hydrogels, conventional aqueous electrolytes, and even organic electrolytes), as illustrated in Fig. 5g [37–65].

To demonstrate the flexibility and adaptability of the MSCs, the CV and GCD curves were tested at various bending angles. Fig. 6a illustrates the MSC device subjected to different bending angles. The CV curves in Fig. 6b retain their shape even as the bending angle increases, indicating robust flexibility. Fig. 6c shows the areal capacitance for different bending angles at 100 mV s^{-1}, with values of 7.91 mF cm^{-2} at 180° and 8.14 mF cm^{-2} when the device is flat, verifying the superior flexibility of the MSCs. In Fig. 6d, the GCD curves show negligible change under different bending angles, which is consistent with the behavior in the CV curves. To meet various operational requirements, inkjet printing processes can enable series or parallel connections of MSCs, tailored for portable applications, and manufactured on alternative substrates such as polyimide, as depicted in Fig. S10. Connecting multiple MSCs in series or parallel can enhance the output voltage and extend the discharge time, as demonstrated in Fig. 6e and f. When two MSCs are connected in series, they exhibit an electrochemical window of 1.2 V on both CV and GCD curves. As shown in Video 1, connecting multiple MSCs in parallel can power LEDs.

To evaluate the temperature tolerance of MSCs, CV curves were obtained at a spectrum of temperatures, as depicted in Fig. S11. Fig. 6g and h displays the CV curves and corresponding areal capacitances at different temperatures at 200 mV s^{-1}. The data demonstrate that the area under the CV curve and the areal capacitance exhibit a decline with a reduction in temperature, which is attributed to increased ion transport resistance resulting from increased electrolyte viscosity and contraction of the hydrogel network at lower temperatures. At the scan rate of 200 mV s^{-1}, the MSCs exhibit areal capacitances of 11 mF cm^{-2} at 80 °C, 7.8 mF cm^{-2} at 20 °C, and 5.4 mF cm^{-2} at −30 °C. The corresponding areal energy densities are 0.55 μWh cm^{-2}, 0.39 μWh cm^{-2}, and 0.27 μWh cm^{-2}, respectively, demonstrating the MSCs can operate across a wide temperature range (−30 to 80 °C). Additionally, EIS measurements of MSCs at different temperatures are presented in Fig. 6i. The series resistance of the MSCs decreases as the temperature increases. The low-frequency Nyquist plots exhibit near-parallel alignment across the temperature range, suggesting stable charge transport in the MSCs under varying temperature conditions. The cyclic stability tests of MSCs at different temperatures are shown in Fig. S12. The MSCs maintain a capacity retention rate exceeding 75.5 % and a coulombic efficiency above 90 % after 8000 cycles at 0.3 mA cm^{-2} across the temperature range (−30 to 80 °C), indicating robust cycle stability in extreme environments. The effective functioning of MSCs under extreme conditions

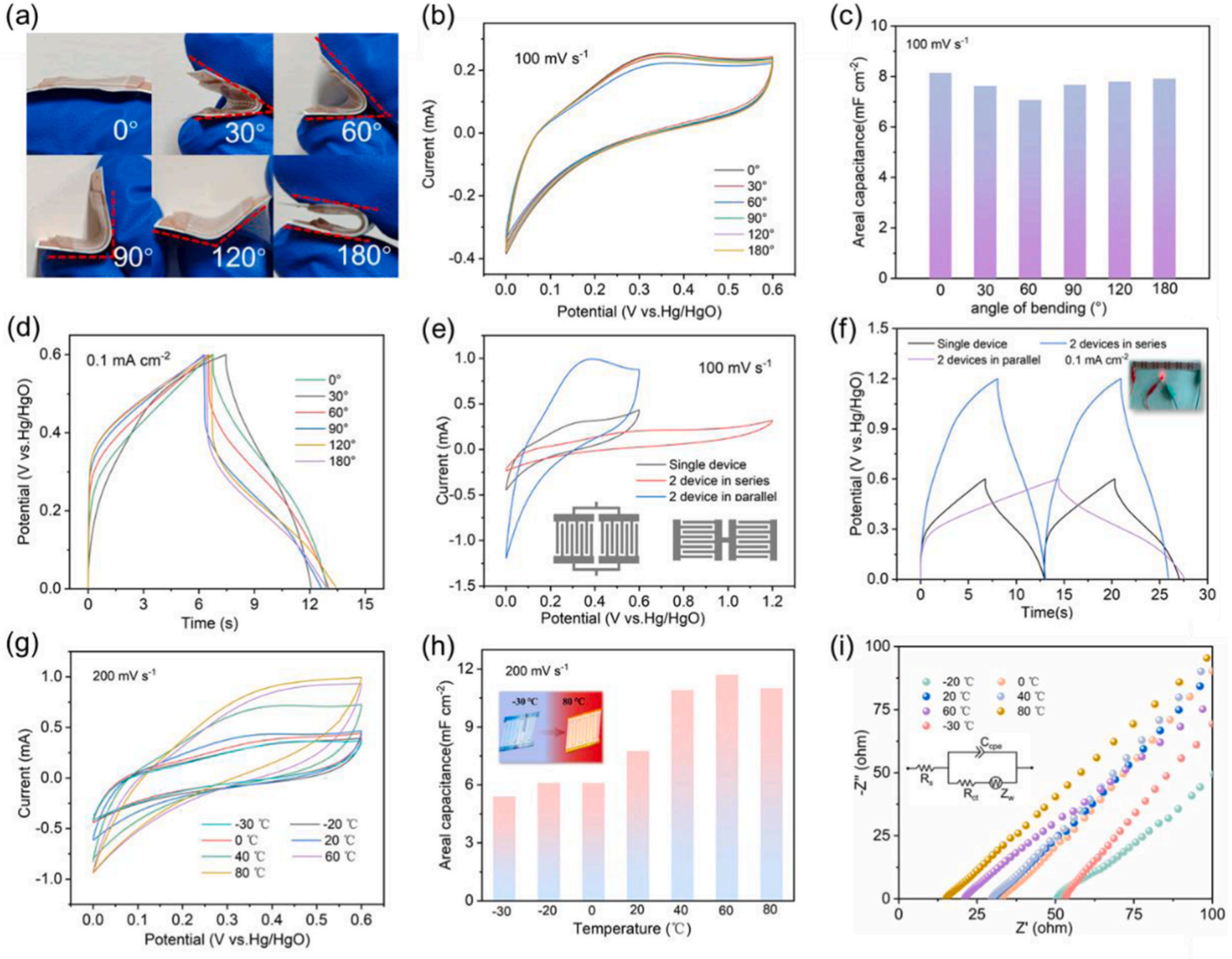

Fig. 6. (a) Optical photographs of MSC at different bending angles. (b) CV curves of MSCs under different bending angles at 100 mV s^{-1}. (c) GCD curves of MSCs under different bending angles at 0.1 mA cm^{-2}. (d) Areal capacity graphs of MSCs under different bending angles at 100 mV s^{-1}. (e) The CV curves at 100 mV s^{-1} and (f) GCD profiles at 0.1 mA cm^{-2} of a single microdevice in series or parallel. (g) CV curves and (h) areal capacity at 200 mV s^{-1} of MSCs under the different temperatures. (i) EIS curves of MSCs under different temperatures.

can be attributed to two main factors: the hydrogen bonds between trehalose and water molecules, which lowers the freezing point of the hydrogel and delays ice formation, and the strong hydration of Li^+ and Cl^- ions, which disrupts the interaction between water molecules, reducing the free water content and increasing the bound water content in the hydrogel. The synergy between the components in the PAM/trehalose/LiCl hydrogel allows it to withstand temperature variations, enabling the MSCs to operate over an extensive temperature range.

3. Conclusion

In conclusion, the development of novel MSCs featuring flower-like 1T-phase MoS_2 assembled on RGO as electrodes, combined with a PAM/trehalose/LiCl hydrogel electrolyte, represents a significant advancement in optimizing electrochemical performance across a broad temperature range. The 1T-MoS_2/RGO electrodes enable the MSCs to achieve an impressive volume energy density of 15.0 mWh cm^{-3} at 20 °C. The PAM/trehalose/LiCl hydrogel confers exceptional flexibility and adaptability to the MSCs, enabling operation within a temperature range from −30 °C to 80 °C. Additionally, the MSCs demonstrate outstanding cycling stability, retaining over 75.5 % of their capacity and more than 90 % of their coulombic efficiency after 8000 cycles across the wide temperature range. Leveraging the simplicity of inkjet printing, MSC devices can be readily interconnected in series or parallel to enhance power output. This achievement offers an effective way to develop flexible energy storage devices with a wide operating temperature range.

CRediT authorship contribution statement

Na Chen: Writing – review & editing, Writing – original draft, Software, Methodology, Investigation, Formal analysis, Data curation. **Guo-Tao Xiang:** Software, Methodology, Investigation, Data curation. **Rui-Dong Shi:** Software, Resources, Data curation. **Jia-Lei Xu:** Supervision, Software, Methodology. **Aura Garcia:** Visualization, Validation, Software. **Raul D. Rodriguez:** Validation, Software. **Jin-Ju Chen:** Writing – review & editing, Funding acquisition.

Declaration of competing interest

No potential conflict of interest was reported by the authors.

Acknowledgments

The work was supported by the Sichuan Science and Technology Program (grant No. 2023YFG0215) and the Chengdu Science and Technology Program (grant No. 2023-GH02-00021-HZ).

Appendix A. Supplementary data

Supplementary data to this article can be found online at https://doi.org/10.1016/j.jpowsour.2025.239162.

Data availability

The data that has been used is confidential.

References

[1] M.R. Islam, S. Afroj, K.S. Novoselov, N. Karim, Inkjet-printed 2D heterostructures for smart textile micro-supercapacitors, Adv. Funct. Mater. 34 (2024) 2410666.

[2] L. Zhang, J. Qin, P. Das, S. Wang, T. Bai, F. Zhou, et al., Electrochemically exfoliated graphene additive-free inks for 3D printing customizable monolithic integrated micro-supercapacitors on a large scale, Adv. Mater. 36 (2024) e2313930.

[3] M. Beidaghi, Y. Gogotsi, Capacitive energy storage in micro-scale devices: recent advances in design and fabrication of micro-supercapacitors, Energy Environ. Sci. 7 (2014).

[4] C. Yang, K.S. Schellhammer, F. Ortmann, S. Sun, R. Dong, M. Karakus, et al., Coordination polymer framework based on-chip micro-supercapacitors with AC line-filtering performance, Angew. Chem. Int. Ed. 56 (2017) 3920–3924.

[5] X. Xu, Z. Lu, L. Hua, J. Dong, Z. Guo, Y. Kou, et al., Entire ultrathin two-dimensional pseudocapacitive nanosheets with high active covalent groups for flexible asymmetric all-solid-state micro-pseudocapacitors with high energy density and long cycle life, J. Colloid Interface Sci. 679 (2025) 643–655.

[6] D. Zhao, W. Chang, C. Lu, C. Yang, K. Jiang, X. Chang, et al., Charge transfer salt and graphene heterostructure-based micro-supercapacitors with alternating current line-filtering performance, Small 15 (2019).

[7] X. Shi, S. Pei, F. Zhou, W. Ren, H.-M. Cheng, Z.-S. Wu, et al., Ultrahigh-voltage integrated micro-supercapacitors with designable shapes and superior flexibility, Energy Environ. Sci. 12 (2019) 1534–1541.

[8] H. Li, S. Liu, X. Li, Z.-S. Wu, J. Liang, Screen-printing fabrication of high volumetric energy density micro-supercapacitors based on high-resolution thixotropic-ternary hybrid interdigital micro-electrodes, Mater. Chem. Front. 3 (2019) 626–635.

[9] S. Zheng, J. Ma, Z.-S. Wu, F. Zhou, Y.-B. He, F. Kang, et al., All-solid-state flexible planar lithium ion micro-capacitors, Energy Environ. Sci. 11 (2018) 2001–2009.

[10] H. Xu, J. Zhu, M. Xu, Z. Lei, Q. Hu, X. Jin, Flexible and alternately layered high electrochemical active electrode based on MXene, carboxymethylcellulose, and carbon nanotube for asymmetric micro-supercapacitors, J. Colloid Interface Sci. 645 (2023) 974–984.

[11] E. Kim, J. Song, T.-E. Song, H. Kim, Y.-J. Kim, Y.-W. Oh, et al., Scalable fabrication of MXene-based flexible micro-supercapacitor with outstanding volumetric capacitance, Chem. Eng. J. 450 (2022).

[12] J. Cao, C. Yan, Z. Chai, Z. Wang, M. Du, G. Li, et al., Laser-induced transient conversion of rhodochrosite/polyimide into multifunctional MnO_2/graphene electrodes for energy storage applications, J. Colloid Interface Sci. 653 (2024) 606–616.

[13] Y. Xie, H. Zhang, X. Jiang, L. Fan, J. Huang, W. Wang, et al., In-situ construction of integrated asymmetric micro-supercapacitors achieving monolithic hundred-volt output, J. Colloid Interface Sci. 677 (2025) 12–20.

[14] P. Sun, J. Liu, Q. Liu, J. Yu, R. Chen, J. Zhu, et al., An inkjet-printing ink based on porous NiS/N-MXene for high-performance asymmetric micro-supercapacitors and self-powered microelectronics, Chem. Eng. J. 474 (2023).

[15] C. Zhang, L. McKeon, M.P. Kremer, S.-H. Park, O. Ronan, A. Seral-Ascaso, et al., Additive-free MXene inks and direct printing of micro-supercapacitors, Nat. Commun. 10 (2019).

[16] R. Yang, Y. Fan, Y. Zhang, L. Mei, R. Zhu, J. Qin, et al., 2D transition metal dichalcogenides for photocatalysis, Angew. Chem. Int. Ed. 62 (2023).

[17] A.T. Garcia-Esparza, S. Park, H. Abroshan, O.A. Paredes Mellone, J. Vinson, B. Abraham, et al., Local structure of sulfur vacancies on the basal plane of monolayer MoS_2, ACS Nano 16 (2022) 6725–6733.

[18] P.S. Kiran, K.V. Kumar, N. Pandit, S. Indupuri, R. Kumar, V.V. Wagh, et al., Scaling up simultaneous exfoliation and 2H to 1T phase transformation of MoS_2, Adv. Funct. Mater. 34 (2024).

[19] L. Kang, S. Liu, Q. Zhang, J. Zou, J. Ai, D. Qiao, et al., Hierarchical spatial confinement unlocking the storage limit of MoS_2 for flexible high-energy supercapacitors, ACS Nano 18 (2024) 2149–2161.

[20] K. Jiang, I.A. Baburin, P. Han, C. Yang, X. Fu, Y. Yao, et al., Interfacial approach toward benzene-bridged polypyrrole film-based micro-supercapacitors with ultrahigh volumetric power density, Adv. Funct. Mater. 30 (2019).

[21] J. Ma, Y. Li, Z. Wang, B. Zhang, J. Du, J. Qin, et al., 2D ultrathin graphene heterostructures for printable high-energy micro-supercapacitors integrated into coplanar flexible all-in-one microelectronics, Mater. Today 74 (2024) 58–66.

[22] K. Zhang, Y. Pang, C. Chen, M. Wu, Y. Liu, S. Yu, et al., Stretchable and conductive cellulose hydrogel electrolytes for flexible and foldable solid-state supercapacitors, Carbohydr. Polym. 293 (2022).

[23] H. Su, Q. Guo, C. Qiao, X. Ji, L. Gai, L. Liu, Lignin-alkali metal ion self-catalytic system initiated rapid polymerization of hydrogel electrolyte with high strength and anti-freezing ability, Adv. Funct. Mater. 34 (2024).

[24] L. Köps, F.A. Kreth, D. Leistenschneider, K. Schutjajew, R. Gläßner, M. Oschatz, et al., Improving the stability of supercapacitors at high voltages and high temperatures by the implementation of ethyl isopropyl sulfone as electrolyte solvent, Adv. Energy Mater. 13 (2022).

[25] R. Zhang, Z. Zhang, P. Xu, J. Xu, Y. Gao, G. Gao, Cellulose nanofiber hydrogel with high conductivity electrolytes for high voltage flexible supercapacitors, Carbohydr. Polym. 326 (2024).

[26] X. Wang, T. Du, X. Dong, H. Huang, M. Qi, Application of advanced wide-temperature range and flame retardant “Leaf-Vein” structured functionality composite quasi-solid-state electrolyte, Energy Storage Mater. 68 (2024).

[27] R. Li, W. Jia, J. Wen, G. Hu, T. Tang, X. Li, et al., MXene/Zwitterionic hydrogel oriented anti-freezing and high-performance zinc-ion hybrid supercapacitor, Adv. Funct. Mater. 34 (2024) 2409207.

[28] P.-Z. Li, N. Chen, A. Al-Hamry, E. Sheremet, R. Lu, Y. Yang, et al., Inkjet-printed MoS_2-based 3D-structured electrocatalysts on Cu films for ultra-efficient hydrogen evolution reaction, Chem. Eng. J. 457 (2023).

[29] B. Gao, Y. Zhao, X. Du, D. Qian, S. Ding, C. Xiao, et al., Modulating trinary-heterostructure of MoS_2 via controllably carbon doping for enhanced electrocatalytic hydrogen evolution reaction, Adv. Funct. Mater. 33 (2023).

[30] S. Hussain, I. Rabani, D. Vikraman, A. Feroze, M. Ali, Y.-S. Seo, et al., MoS_2@X_2C (X = Mo or W) hybrids for enhanced supercapacitor and hydrogen evolution performances, Chem. Eng. J. 421 (2021).

[31] L. Wang, F. Liu, B. Zhao, Y. Ning, L. Zhang, R. Bradley, et al., Carbon nanobowls filled with MoS_2 nanosheets as electrode materials for supercapacitors, ACS Appl. Nano Mater. 3 (2020) 6448–6459.

[32] H. Xia, L. Zan, P. Yuan, G. Qu, H. Dong, Y. Wei, et al., Evolution of stabilized 1T-MoS_2 by atomic-interface engineering of 2H-MoS_2/Fe-N_x towards enhanced sodium ion storage, Angew Chem. Int. Ed. Engl. 62 (2023) e202218282.

[33] Z. Liu, K. Nie, X. Qu, X. Li, B. Li, Y. Yuan, et al., General bottom-up colloidal synthesis of nano-monolayer transition-metal dichalcogenides with high 1T’-phase purity, J. Am. Chem. Soc. 144 (2022) 4863–4873.

[34] C. Li, C. Liu, Y. Wang, Y. Lu, L. Zhu, T. Sun, Drastically-enlarged interlayer-spacing MoS_2 nanocages by inserted carbon motifs as high performance cathodes for aqueous zinc-ion batteries, Energy Storage Mater. 49 (2022) 144–152.

[35] G. Chen, J. Huang, J. Gu, S. Peng, X. Xiang, K. Chen, et al., Highly tough supramolecular double network hydrogel electrolytes for an artificial flexible and low-temperature tolerant sensor, J. Mater. Chem. A 8 (2020) 6776–6784.

[36] C. Wang, Y. Liu, X. Qu, B. Shi, Q. Zheng, X. Lin, et al., Ultra-sretchable and fast self-healing ionic hydrogel in cryogenic environments for artificial nerve fiber, Adv. Mater. 34 (2022) e2105416.

[37] K. Thiyagarajan, W.-J. Song, H. Park, V. Selvaraj, S. Moon, J. Oh, et al., Electroactive 1T-MoS_2 fluoroelastomer ink for intrinsically stretchable solid-state in-plane supercapacitors, ACS Appl. Mater. Interfaces 13 (2021) 26870–26878.

[38] C. Xu, L. Jiang, X. Li, C. Li, C. Shao, P. Zuo, et al., Miniaturized high-performance metallic 1T-Phase MoS_2 micro-supercapacitors fabricated by temporally shaped femtosecond pulses, Nano Energy 67 (2020).

[39] S.-W. Kim, J. Hwang, S.-J. Ha, J.-E. Lee, J.-C. Yoon, J.-H. Jang, Ultrathin MoS_2 flakes embedded in nanoporous graphene films for a multi-functional electrode, J. Mater. Chem. A 9 (2021) 928–936.

[40] Y. Yang, L. He, C. Tang, P. Hu, X. Hong, M. Yan, et al., Improved conductivity and capacitance of interdigital carbon microelectrodes through integration with carbon nanotubes for micro-supercapacitors, Nano Res. 9 (2016) 2510–2519.

[41] L. Liu, D. Ye, Y. Yu, L. Liu, Y. Wu, Carbon-based flexible micro-supercapacitor fabrication via mask-free ambient micro-plasma-jet etching, Carbon 111 (2017) 121–127.

[42] B. Li, N. Hu, Y. Su, Z. Yang, F. Shao, G. Li, et al., Direct inkjet printing of aqueous inks to flexible all-solid-state graphene hybrid micro-supercapacitors, ACS Appl. Mater. Interfaces 11 (2019) 46044–46053.

[43] P. Wang, H. Zeng, J. Zhu, Q. Gao, Micro-supercapacitors based on ultra-fine PEDOT: PSS fibers prepared via wet-spinning, Chem. Eng. J. 484 (2024).

[44] P. Sundriyal, S. Bhattacharya, Scalable micro-fabrication of flexible, solid-state, inexpensive, and high-performance planar micro-supercapacitors through inkjet printing, ACS Appl. Energy Mater. 2 (2019) 1876–1890.

[45] J. Jung, J.R. Jeong, C. DangVan, K. Kang, M.H. Lee, Laser-assisted patterning of Co-Ni alloy/reduced graphene oxide composite for enhanced micro-supercapacitor performance, ACS Appl. Electron. Mater. 4 (2022) 4840–4848.

[46] L. Naderi, S. Shahrokhian, Wire-type flexible micro-supercapacitor based on MOF-Assisted sulfide nano-arrays on dendritic CuCoP and V_2O_5-polypyrrole/nanocellulose hydrogel, Chem. Eng. J. 476 (2023).

[47] S. Wang, Z.-S. Wu, F. Zhou, X. Shi, S. Zheng, J. Qin, et al., All-solid-state high-energy planar hybrid micro-supercapacitors based on 2D VN nanosheets and Co$(OH)_2$ nanoflowers, npj 2D Materials and Applications 2 (2018).

[48] S. Chen, H. Sun, Y. Chen, Q. Fang, Z. Huang, Y. Liu, et al., Facile preparation of high-performance free-standing micro-supercapacitors by optimizing oxygen groups on graphene, Small 20 (2024) 2404307.

[49] H. Dong, J. Cao, Y. Ding, S. Wei, Z. Guo, L. Zhang, et al., Bifunctional polyoxometalate clusters-modified single-walled carbon nanotubes for high-energy–density micro-supercapacitors, Chem. Eng. J. 495 (2024).

[50] W. Liu, D. Luo, M. Zhang, J. Chen, M. Li, A. Chen, et al., Engineered MXene quantum dots for micro-supercapacitors with excellent capacitive behaviors, Nano Energy 122 (2024).

[51] E. Yang, X. Shi, L. Wu, H. Zhang, H. Lin, H. Liu, et al., A low-cost moderate-concentration hybrid electrolyte of introducing $CaCl_2$ and ethylene glycerol enables low-temperature and high-voltage micro-supercapacitors, Adv. Funct. Mater. 34 (2024).

[52] S. Wang, L. Li, S. Zheng, P. Das, X. Shi, J. Ma, et al., Monolithic integrated micro-supercapacitors with ultra-high systemic volumetric performance and areal output voltage, Natl. Sci. Rev. 10 (2023).

[53] Z. Liu, Y. Hu, W. Zheng, C. Wang, W. Baaziz, F. Richard, et al., Untying the bundles of solution-synthesized graphene nanoribbons for highly capacitive micro-supercapacitors, Adv. Funct. Mater. 32 (2022).

[54] Y. Xie, H. Zhang, H. Huang, Z. Wang, Z. Xu, H. Zhao, et al., High-voltage asymmetric MXene-based on-chip micro-supercapacitors, Nano Energy 74 (2020).

[55] H. Huang, J. He, Z. Wang, H. Zhang, L. Jin, N. Chen, et al., Scalable, and low-cost treating-cutting-coating manufacture platform for MXene-based on-chip micro-supercapacitors, Nano Energy 69 (2020).

[56] X. Chu, G. Chen, X. Xiao, Z. Wang, T. Yang, Z. Xu, et al., Air-stable conductive polymer ink for printed wearable micro-supercapacitors, Small 17 (2021).

[57] Y. Wu, J. Chen, W. Yuan, X. Zhang, S. Bai, Y. Chen, et al., Direct mask-free fabrication of patterned hierarchical graphene electrode for on-chip micro-supercapacitors, J. Mater. Sci. Technol. 143 (2023) 12–19.

[58] M. Chen, X. Shi, X. Wang, H. Liu, S. Wang, C. Meng, et al., Low-temperature and high-voltage planar micro-supercapacitors based on anti-freezing hybrid gel electrolyte, J. Energy Chem. 72 (2022) 195–202.

[59] P. Sun, J. Liu, Q. Liu, J. Yu, R. Chen, J. Zhu, et al., Nitrogen and sulfur Co-doped MXene ink without additive for high-performance inkjet-printing micro-supercapacitors, Chem. Eng. J. 450 (2022).

[60] Delekta S. Sollami, K.H. Adolfsson, N. Benyahia Erdal, M. Hakkarainen, M. Ostling, J. Li, Fully inkjet printed ultrathin microsupercapacitors based on graphene electrodes and a nano-graphene oxide electrolyte, Nanoscale 11 (2019) 10172–10177.

[61] H. Li, Y. Hou, F. Wang, M.R. Lohe, X. Zhuang, L. Niu, et al., Flexible all-solid-state supercapacitors with high volumetric capacitances boosted by solution processable MXene and electrochemically exfoliated graphene, Adv. Energy Mater. 7 (2016).

[62] P. Das, L. Zhang, S. Zheng, X. Shi, Y. Li, Z.-S. Wu, Rapid fabrication of high-quality few-layer graphene through gel-phase electrochemical exfoliation of graphite for high-energy-density ionogel-based micro-supercapacitors, Carbon 196 (2022) 203–212.

[63] L. Chi, S. Zheng, J. Ma, Y. Liu, F.-F. Xing, F. Zhou, et al., 1.6 V high-voltage aqueous symmetric micro-pseudocapacitors based on two-dimensional polypyrrole/graphene nanosheets, Carbon 194 (2022) 240–247.

[64] J. Ma, S. Zheng, Y. Cao, Y. Zhu, P. Das, H. Wang, et al., Aqueous MXene/PH1000 hybrid inks for inkjet-printing micro-supercapacitors with unprecedented volumetric capacitance and modular self-powered microelectronics, Adv. Energy Mater. 11 (2021).

[65] M.B. Poudel, H.J. Kim, Confinement of zn-mg-al-layered double hydroxide and α-Fe_2O_3 nanorods on hollow porous carbon nanofibers: a free-standing electrode for solid-state symmetric supercapacitors, Chem. Eng. J. 429 (2022).